

## Hydrocarbon Fuels in Solid Oxide Fuel Cells: In Situ Raman Studies of Graphite Formation and Oxidation

Michael B. Pomfret,<sup>†</sup> Jonathan Marda,<sup>‡</sup> Gregory S. Jackson,<sup>§</sup> Bryan W. Eichhorn,<sup>†</sup> Anthony M. Dean,<sup>‡</sup> and Robert A. Walker<sup>\*,†</sup>

Department of Chemistry and Biochemistry, University of Maryland, College Park, College Park, Maryland 20742, Department of Chemical Engineering, Colorado School of Mines, Golden, Colorado 80401, and Department of Mechanical Engineering, University of Maryland, College Park, College Park, Maryland 20742

Received: November 29, 2007; In Final Form: January 11, 2008

In situ Raman spectroscopy and linear sweep voltammetry were used to characterize graphite formation on Ni/YSZ cermet anodes in solid oxide fuel cells (SOFCs) operating at 715 °C. The membrane electrode assemblies were run continuously with Ar-diluted H<sub>2</sub> and exposed to intermittent bursts of hydrocarbons. The appearance and disappearance of carbon deposits was monitored as a function of cell potential and hydrocarbon fuel identity. The hydrocarbon fuels employed in these studies included methane, ethylene, and propylene. Kinetic modeling predicts that of these three fuels, propylene is the most reactive under the conditions of the SOFC experiments. Methane was predicted to be virtually unreactive in the gas phase. Limited exposure of the SOFC anode to methane led to no observable carbon deposits and no appreciable change in SOFC electrochemical performance. Extended exposure to a continuous methane feed resulted in the formation of highly ordered graphite as evidenced by a single feature (assigned as the “G” band) at 1585 cm<sup>-1</sup> in the Raman spectrum. The addition of ethylene to the incident fuel leads initially to the formation of highly ordered graphite as evidenced by the rapid growth of the G band and a small “D” band (at 1365 cm<sup>-1</sup>) in the Raman spectrum. Subsequent additions of ethylene created more disorder and led to deteriorating SOFC performance. Small amounts of propylene added to the fuel feed formed disordered carbon having significant amounts of tetrahedrally coordinated carbon, and SOFC performance suffered reversible degradation. Applying an overpotential to the anode led to the disappearance of carbon deposits with the intensity of the D band diminishing more rapidly than the G band. The disappearance rates depended directly on the anode overpotential.

### Introduction

Solid oxide fuel cells (SOFCs) offer tremendous potential for clean, high-efficiency power generation.<sup>1–5</sup> Unlike low-temperature proton-exchange membrane fuel cells (PEMFCs), SOFCs with their high operating temperatures have the potential to convert a wide range of fuels—not just molecular hydrogen—into electricity and simple chemical byproducts.<sup>6–10</sup> Despite the versatility of SOFCs compared to other devices, however, the porous anode structures often used in conventional SOFC architectures are still susceptible to carbon deposition from hydrocarbon fuels.<sup>11,12</sup> Excessive carbon formation represents a primary mechanism for anode destruction and, ultimately, device failure.<sup>13–16</sup>

Two mechanisms have been proposed as the origin of deposit formation. First, gas-phase reactions can lead to production of high molecular weight species (e.g., aromatics) that serve as deposit precursors.<sup>32</sup> Second, catalytic surface chemistry mechanisms, such as those involving elemental nickel (Ni), the most common anode electrocatalyst, involve C–H bond activation and subsequent graphite formation under appropriate conditions.<sup>11,17–23</sup> To avoid carbon formation on porous, Ni-based anodes, particularly those exposed to higher-molecular-weight

hydrocarbon fuels, adequate oxidizing agents must be present in the form of oxide ions that migrate through the electrolyte to the electrochemically active region and/or steam formed from hydrocarbon oxidation or added intentionally to the fuel inlet.<sup>24,25</sup> Progress in limiting the adverse effects of carbon deposition has resulted from functionally graded porous anode structures with outer diffusion barriers that promote improved hydrocarbon steam reforming by increasing the water product concentration within the porous media.<sup>26–29</sup>

Understanding the mechanisms responsible for carbon deposit formation on SOFC anodes is limited by uncertainty concerning the molecular species present in the gas phase as well as on the electrocatalyst and electrolyte surfaces. Most hydrocarbon fuels undergo extensive pyrolysis at the high temperatures necessary for SOFC operation, typically 650–900 °C.<sup>12,30–32</sup> For example, at temperatures above 650 °C, butane undergoes gas-phase pyrolysis to form smaller saturated and unsaturated hydrocarbons as well as larger graphitic precursors.<sup>32</sup> Such a heterogeneous mixture leads to multiple pathways for fuel electrooxidation as well as carbon deposition. Furthermore, pyrolysis product distributions have been shown to depend sensitively on system temperature and fuel composition and residence times.<sup>30,32–34</sup> Coupled chemical mechanisms resulting from heterogeneous fuel mixtures introduce additional complications to efforts intended to model SOFC kinetics, efficiency, and durability.

The general lack of molecularly specific data acquired from operating SOFCs presents a critical impediment to understanding

\* To whom correspondence should be addressed.

<sup>†</sup> Department of Chemistry and Biochemistry, University of Maryland.

<sup>‡</sup> Colorado School of Mines.

<sup>§</sup> Department of Mechanical Engineering, University of Maryland.

the chemistry occurring on SOFC anodes. Newly developed kinetic models appear to describe accurately the gas-phase chemistry occurring prior to a hydrocarbon fuel reaching the SOFC anode,<sup>35,36</sup> but the subsequent heterogeneous chemistry occurring on anode surfaces remains poorly understood. Voltammetry and electrochemical impedance spectroscopy (EIS) can show clearly how cell performance responds to varying conditions,<sup>7,37–39</sup> but results from these measurements do not reveal the molecular origins of observed changes. Furthermore, ex situ studies can correlate changes to anode structure and composition with sequences of controlled operations but only after the device has been cooled and disassembled.<sup>26–29,40</sup> Quantitative, predictive models of electrochemical oxidation in SOFCs require real-time, in situ information about specific species present on and near SOFC anodes under typical operating conditions.

Recently, Raman spectroscopy has emerged as a promising in situ tool for probing processes in operating SOFCs.<sup>18,41–43</sup> Raman spectroscopy measures vibrational transitions, meaning that the technique is inherently sensitive to molecular and material identity. By examining vibrational band intensities and frequencies, one can directly observe molecular structure as well as interactions between species. Furthermore, with the appropriate choice of excitation wavelength, one can avoid the blackbody background problems that plague traditional IR absorbance-based measurements.<sup>44</sup>

The experiments described below study carbon formation and the subsequent electrochemical oxidation on SOFC anodes operating with various hydrocarbon fuels. Raman spectroscopy is used to characterize in situ the carbon formed on Ni/YSZ cermet anodes in SOFCs operating at 715 °C. The effect of cell potential on the oxidation of the deposits is characterized using timed-acquisition Raman spectra. The hydrocarbon fuels used in these studies, methane, ethylene, and propylene, were chosen because they represent the primary components of butane pyrolysis (accounting for nearly 90% of the carbon products found in a butane feed that has passed through a 700 °C quartz reactor in 5 s).<sup>32</sup> Butane is often used as a simple “heavy” hydrocarbon fuel, and previous studies examining SOFCs operated with butane have shown that the early stages of carbon formation on electrocatalytic anodes can have nonintuitive effects on SOFC performance.<sup>37,42,45,46</sup> Spectroscopic data presented in this work show that smaller hydrocarbon fuels lead to distinctly different types of carbon deposits on Ni/YSZ cermet anodes. Simultaneous electrochemical measurements provide direct comparisons between the carbon formed on the anode and overall device performance. Correlations between the different types of carbon deposits formed from different hydrocarbon fuels and SOFC performance characterized by voltammetry measurements imply that no single gas-phase species is responsible for the cell behavior observed with the complex pyrolysis mixtures formed by butane and higher-weight hydrocarbon fuels.

## Experimental Section

**Fuel Cell Construction.** The SOFC electrolytes were constructed using yttria stabilized zirconia (YSZ) powder acquired commercially from Tosoh. The YSZ contained 8% yttria (by mole fraction of Y relative to Zr). A mass of 2.0 g of the powder was pressed at 20 000 psi for 10 min and then sintered at 1500 °C for 1 h with a heating and cooling rate of 1 °C per minute. The resulting electrolyte disks had diameters of 25 mm and thicknesses of 0.80 mm. Porous anodes were made using Ni/YSZ paste (50% Ni, 50% YSZ by weight, post-reduction)

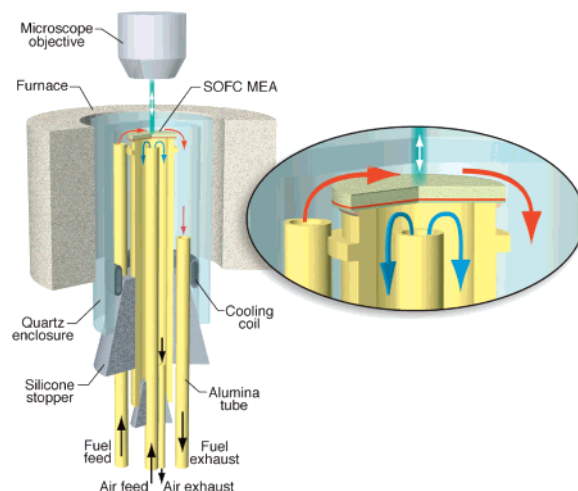


**Figure 1.** Schematic showing the optically accessible, electrochemical rig used to acquire Raman data from SOFCs operated at 715 °C.

acquired from NexTech Materials (Lot No. 112-45). The 12.5 mm diameter anodes were painted onto the center of the electrolyte disk with a Kapton-tape mask and then sintered at 1300 °C for 3 h with heating and cooling rates of 1 °C per min, resulting in anode thicknesses of  $\sim 20$   $\mu\text{m}$ . Porous cathodes were made from a LSM/YSZ (50%  $\text{La}_{0.85}\text{Sr}_{0.15}\text{MnO}_3$  and 50% YSZ by weight) paste made in-house. The paste was painted in a 12.5 mm diameter area opposite the anode and sintered. The sintering procedure for the cathode was multisteped and included heating to 400 °C at 0.33 °C per min, holding the temperature at 400 °C for 1 h, heating to 1300 °C at 1 °C per min, holding the temperature at 1300 °C for 1 h, and cooling to room temperature at 3 °C per min.

Gold wires were attached to the anodes and cathodes of the completed membrane-electrode assemblies using Au ink (Engelhard No. A1644) and Pt ink (Engelhard No. 6926), respectively. The wired disks were attached anode-side-out to an alumina tube assembly with zirconia paste. A quartz tube ( $\sim 40$  cm), closed on one end, surrounded the alumina-supported MEA to contain the reactant and product gases and provide optical access to the anode. The cathode and anode inlet flow ports were sealed with tapered, silicone rubber plugs. A split-tube furnace (ThermCraft) was fitted around the upper two-thirds of the assembly and heated to a temperature of 1000 °C while the bottom was cooled by water and compressed air to preserve seals. A schematic of the assembled fuel cell is shown in Figure 1.

**Gas Flows.** Fuel flows must be regulated to keep the optical window clean while a constant cell polarization is applied. To sustain constant cell voltage, an argon/hydrogen feed mixture was used (150 sccm Ar, 30 sccm  $\text{H}_2$ ). To observe the effect of adding hydrocarbons to this feed, a “hydrocarbon burst” was introduced at a flow rate of 30 sccm for 10 s to the base Ar/ $\text{H}_2$  flow. In this manner, the SOFC was exposed to 5  $\text{cm}^3$  of the specified hydrocarbon. This technique allows for the investigation of the effects of cell exposure to hydrocarbons on a well-resolved time scale. The presence of  $\text{H}_2$  is expected to limit the amount of carbon deposited.<sup>47,48</sup> For electrochemical data collection, the anode-side flow was 150 sccm Ar and 100 sccm  $\text{H}_2$ . In the case of a constant methane flow, the fuel feed was 150 sccm for Ar and 25 sccm for methane. At a rate of 90 sccm, air was flowed over the cathode during all measurements. Rotameters (Omega) regulated flow rates with precisions of  $\pm 1$  sccm, and all experiments described in this work use “dry” (i.e., nonhumidified) gases. Because the total pressure inside

the anode chamber was approximately 1.0 atm, the partial pressures of the gases are approximately equivalent to ratios of their respective flow rates. For example, the partial pressure of  $H_2$  is 0.4 atm and that of Ar is 0.6 atm during electrochemical measurements, and the initial partial pressures of  $H_2$ , hydrocarbon, and Ar are 0.14, 0.14, and 0.72 atm, respectively, during the time that hydrocarbons are introduced to the operating SOFC.

Before reaching the anode, the fuel mixture passes through the length of the furnace ( $\sim 25$  cm) surrounding the SOFC assembly. This path subjects the fuel to a very steep temperature gradient: the mixture enters the assembly at room temperature, passes through the middle zone of the furnace where the temperature climbs to 1000 °C, and emerges from the feed tube at the anode where the temperature is 715 °C. The fuel inlet itself is a thin alumina tube (3 mm i.d.) attached to the outside of the tube supporting the MEA. The total time required for the fuel mixture to traverse this gradient as estimated by the model described below is  $\sim 0.20$  s (0.18 s for butane) with  $\sim 0.03$  s spent in the “hot” zone of the furnace above 900 °C.

To account for any gas-phase chemistry that occurs in the fuel mixture prior to the anode, the hydrocarbon pyrolysis was modeled for a geometry that closely approximated the temperature-time history in the experimental assembly. The mechanism used consists of 1403 reactions and 205 species and is a modified version of the mechanism used by Sheng and Dean.<sup>32</sup> The details of these modifications have been described by Randolph and Dean.<sup>36</sup> These models have been shown to accurately predict both extent of conversion and major product distributions for pyrolysis of *n*-butane and *n*-hexane. Thus, we expect that predictions for these cases will yield reasonable estimates of the gas mixture composition as it exits the feed tube and impinges upon the anode.

**Electrochemical Characterization.** Cell polarization and electrochemical measurements were taken by a Gamry Instruments PCI4 potentiostat/galvanostat/ZRA. Cells were polarized at three voltages: open circuit voltage (OCV or 1.05 V), 0.75, and 0.45 V. Maximum current densities of  $\sim 25$  mA/cm<sup>2</sup> were measured for cells operating with  $H_2$  prior to exposure to hydrocarbons. Current densities were limited by the electrolyte thickness and the relatively low operating temperature. Throughout this text, descriptions of cell operating conditions will refer to cell potentials in terms of magnitude relative to OCV. In other words, cells operated at “low” potential (such as 0.45 V) correspond to relatively high currents ( $\sim 50\%$  of  $I_{\max}$ ). Similarly, 0.75 V corresponds to lower current ( $\sim 20\%$   $I_{\max}$ ) and a cell voltage closer to that at OCV. The use of dry  $H_2$  led to some variability in the measured OCV. This sensitivity results from the fact that OCV conditions reflect a balance between reactants ( $H_2$ ,  $O^{2-}$ ) and products ( $H_2O$ ) due to the dependence of the Nernst equation on the equilibrium constant. The very low partial pressures of  $H_2O(g)$  in the anode chamber meant that the measured OCV was susceptible to very small changes in the denominator of  $K_{eq}$ .<sup>49</sup> Low OCV conditions can also reflect the presence of leakage current (through the cell) or an oxidant (such as air in the fuel lines). Given the stability of carbon deposits formed by carbon-containing fuels on anodes at OCV, we believe these alternative explanations do not pertain to the systems described below.

Typically, the OCV values with  $H_2$  measured for cells in these studies ranged between 1.05 and 1.10 V. During the course of an individual series of experiments (carried out using the same cell), OCV values varied by less than 0.02 V. Voltammetry and EIS measurements made periodically during the Raman experi-

ments ensured stable cell operation. Experiments measuring the effects of carbon deposits on SOFC performance left cells at OCV during hydrocarbon exposure in order to prevent subsequent oxidation of the initial deposits. Voltammetry measurements were made after the 5th, 10th, and 15th “bursts”. Linear voltammetry sweeps with only  $H_2$  as the fuel were conducted from OCV to 0.00 V cell potential at an effective scan rate of 10 mV/s and a step size of 20 mV. Losses attributed to the electrolyte are subtracted from each  $V-I$  plot.<sup>50</sup> We note that data shown in the  $V-I$  plots (Figure 9) are the results from individual cells. All experiments were repeated on at least three separate occasions using new SOFC assemblies. Quantitative details (i.e., maximum power and current densities) varied by  $\pm 5$ –10% from cell to cell—an effect we attribute to variable microstructure of the anode and/or cathode cermet—but the trends in relative performance as a function of exposure to carbon were reproduced quantitatively with each experiment.

**Raman Measurements.** Raman spectra were acquired with a Renishaw In-Via Raman microscope using a custom-built optical accessory that allowed the microscope objective lens to be lowered into the furnace to focus the incident beam on the anode surface. The objective was cooled by compressed air. Samples were irradiated with the 488 nm output of an Ar<sup>+</sup> ion laser (25 mW) focused to a 1  $\mu$ m sized spot. For each fuel, Raman spectra of the anode surface were acquired immediately before exposure to the hydrocarbon (30 s scans) and every minute for the first 4 min after exposure (30  $\times$  1 s scans for each). This measurement was followed immediately by a 200 s scan for improved signal-to-noise (S/N) ratio spectra of any species that remained on the anode surface. As with the VI data, each experiment was repeated a minimum of three (and as many as five) times with different cell assemblies. The behavior observed in deposit growth and disappearance as well as deposit structure was reproduced during each and every experiment.

The spectra presented in the next section show two features associated with the formation of graphitic carbon. The vibrational band at 1585 cm<sup>-1</sup> arises from extended domains of highly ordered graphite and is generally labeled “G” (for graphite) or by its symmetry,  $E_{2g}$ .<sup>51</sup> The band at 1365 cm<sup>-1</sup>, labeled in most references as either “D” or  $A_{1g}$ , is much broader and corresponds to tetrahedral carbon defects within a graphite lattice.<sup>51</sup> Some reports associate this low-frequency feature explicitly with “disorder”,<sup>52–54</sup> although this disorder could result from a multitude of sources such as grain boundaries, point vacancies, or chemical heterogeneity. In the discussion below, G and D labels are used to assign features of carbon deposits formed on Ni/YSZ anodes from carbon-containing gas-phase fuels. When interpreting the magnitude of the D band in terms of the type of carbon formed, we use the term “disorder” to refer explicitly to carbon that disrupts the extended,  $sp^2$  bonding characteristic of highly ordered graphite.

## Results and Discussion

**Gas-Phase Composition of Fuel Mixtures.** Methane, ethylene, and propylene were introduced into SOFCs operating at three different cell potentials using the “burst” technique. Given the propensity of hydrocarbons (other than methane) to undergo gas-phase pyrolysis at temperatures above 700 °C, the composition of the fuel mixture impinging on the anode can be considerably different than what is introduced originally. Figure 2 shows the predicted decrease in concentration of the fuel as it traverses through the furnace (plotted as the fraction of the original fuel that remains unreacted). These values have been corrected for any increase in the number of moles due to



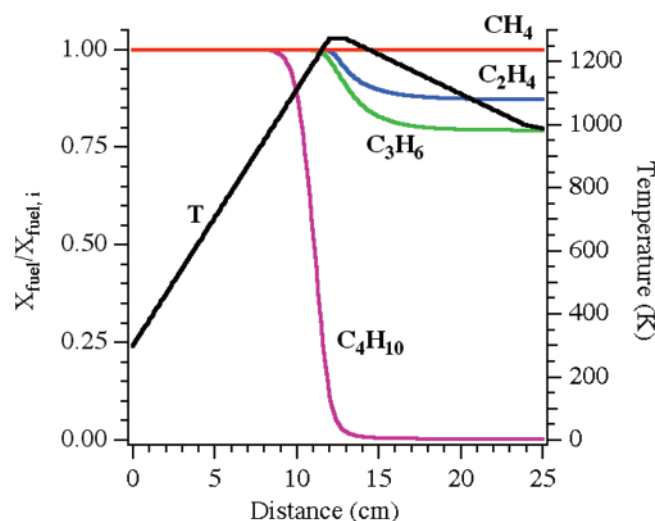


**Figure 2.** Predicted profiles of the ratio of remaining fuel to initial values as the fuel traverses the furnace and is subjected to pyrolysis for methane, ethylene, propylene, and butane.

reaction so that they reflect the decrease in mole fraction of the parent fuel due only to reaction. The final value (at  $x = 25$  cm) is the fraction of the parent fuel that is predicted to be unreacted at the anode location. Also plotted in Figure 2 (against the right axis) is the assumed temperature profile of the fuel feed line. Not surprisingly, the fuel mixture containing a burst of methane is predicted to remain largely unchanged. The model predictions also show that the ethylene mole fraction has decreased to 87% of its original value at the anode location. The propylene mole fraction is predicted to drop to 79% of its original value. Butane is predicted to be much more reactive; it is completely consumed well before encountering the anode.

For those species undergoing pyrolysis, two questions arise. First, what are the product distributions resulting from pyrolysis? Second, does pyrolysis lead to the formation of higher-weight species that can serve as deposit precursors or nucleating sites for carbon deposits on the SOFC anode? Figure 3 shows the predicted product distributions for ethylene, propylene, and butane. For ethylene, the primary products are acetylene, 1,3-butadiene, and ethane with smaller amounts of methane and vinylacetylene. Methane, ethylene, and acetylene are predicted to be the dominant products of propylene pyrolysis, with smaller amounts of methyl acetylene and allene formed. Butane pyrolysis yields ethylene and methane as major products, followed by propylene, acetylene, and methyl acetylene. The product mole fractions from butane pyrolysis are substantially larger than for the other fuels, reflecting the much larger extent of conversion. An important point to note is that the dominant products arising from butane pyrolysis are the same three fuels studied individually in the present experiments.

The gas-phase pyrolysis predictions also indicate formation of higher-molecular-weight species that might serve as deposit precursors. The sums of all the species with molecular weights higher than butane are used as a measure of this deposit propensity and are designated collectively as “ $\text{C}_5^+$ ”. These values are shown in Figure 4. The amount of deposit precursors increases by almost an order of magnitude in going from ethylene to butane. The predicted larger concentration of deposit precursors with butane is consistent with previous in situ observations of rapid build up of disordered carbon on Ni/YSZ anodes.<sup>40</sup> However, if we consider deposit formation on the basis of the number of carbon atoms in the deposit precursors versus the number of carbon atoms reacted, a different picture emerges.

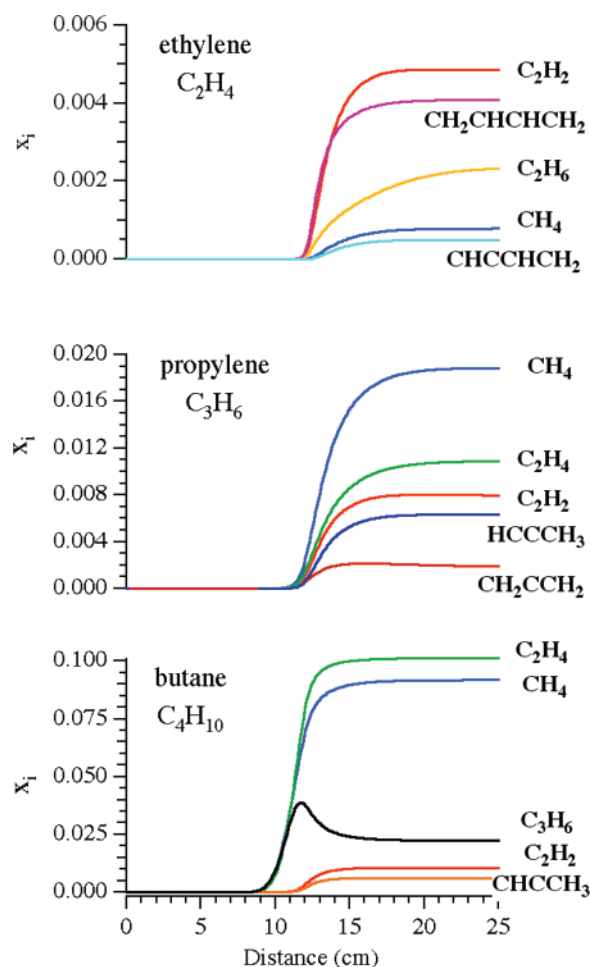


**Figure 3.** Predicted mole fraction profiles of pyrolysis products of ethylene (top), propylene (middle), and butane (bottom) plotted as a function of distance along the fuel inlet. Only the top five product species are shown.

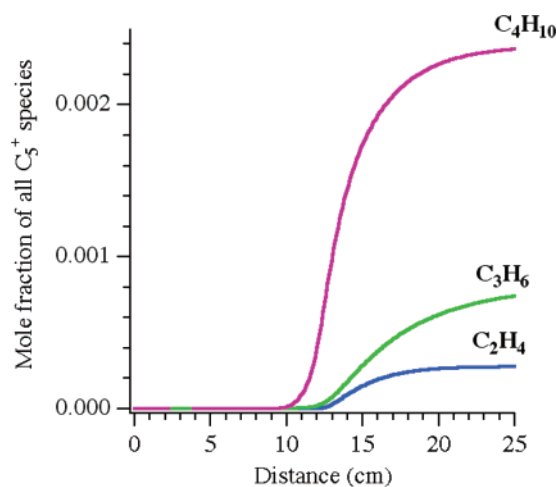


**Figure 4.** Predicted mole fraction profiles of  $\text{C}_5^+$  species present in the post-pyrolysis flows of ethylene, propylene, and butane.

Ethylene and propylene have similar selectivities to the formation of deposit precursors: With ethylene the amount of carbon reacted that resides in deposit precursors (i.e.,  $\text{C}_5^+$ ) is  $\sim 4.3\%$  and for propylene it is  $\sim 4.1\%$ . However, butane selectivity is significantly lower at  $\sim 2.2\%$ . The difference is likely due to the larger concentration of unsaturated species in the ethylene and propylene mixtures; such species promote growth through radical addition reactions. The different structure of the fuels is

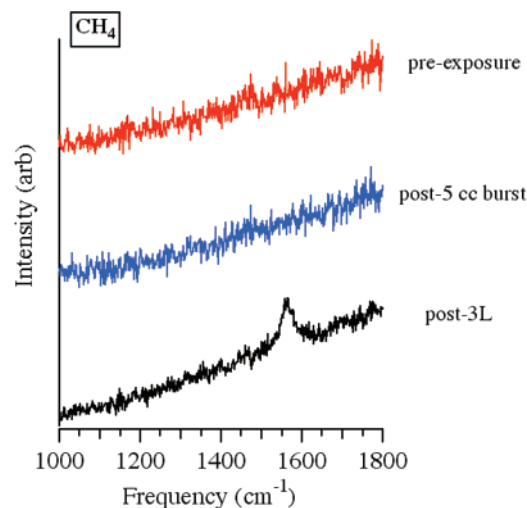


**Figure 5.** Raman spectra acquired from a Ni/YSZ porous anode prior to exposure to CH<sub>4</sub> (top), after exposure to 5 cm<sup>3</sup> of CH<sub>4</sub> (middle), and after exposure to 3 L of CH<sub>4</sub> (bottom). All measurements were made at OCV and at a temperature of 715 °C.

also manifested in the nature of the C<sub>5</sub><sup>+</sup> species produced. For ethylene, the dominant product is benzene. Propylene forms mostly 1,3-cyclopentadiene, reflecting the significant concentration of both C<sub>3</sub> and C<sub>2</sub> unsaturated species in this reacting system. Butane forms 1,3-cyclopentadiene, fulvene, and benzene, reflecting the more complex mix of unsaturated species in this system.

An important point to remember when considering the heterogeneous mixtures predicted from pyrolysis of the hydrocarbons in the fuel feed is that the model explicitly includes the molecular hydrogen present during all experimental studies. Hydrogen is expected to retard the rate of PAH growth in gas-phase carbon mixtures, and the product distributions (including C<sub>5</sub><sup>+</sup> populations) are expected to change significantly in the absence of hydrogen. How these changes impact the amount of carbon deposited on SOFC anodes (and the resulting carbon structure) is the subject of ongoing studies.

**Potential Dependence of Carbon Deposition.** Figure 5 shows in situ Raman spectra of systems exposed to methane. The top, featureless trace results from a 30 s scan of the clean anode operating with a hydrogen/argon feed. Exposure to 5 cm<sup>3</sup> of methane (or  $\sim 2.0 \times 10^{-4}$  mol) at 1.05 V (OCV) led to no measurable Raman signal, indicating a lack of detectable carbon deposits on the anode (middle trace, Figure 5). Carbon also fails to deposit with methane exposure under moderate and high current conditions (corresponding to cell potentials of 0.75 and 0.45 V, respectively, as shown in the Supporting Information (Figure S1)). While the absence of carbon deposits under typical operating conditions (with O<sub>2</sub><sup>2-</sup> fluxes from the electrolyte and H<sub>2</sub>O generation) should not be surprising, the lack of carbon deposition on the Ni/YSZ anode with methane at OCV contrasts dramatically with the behavior observed with higher-weight hydrocarbon fuels (vide infra). The modeling results presented above indicate that the gas-phase pyrolysis of methane is unlikely to form deposit precursors.

The OCV observations also indicate that the short burst of methane was also insufficient to form deposits catalytically on the anode surface. Only after prolonged exposure (25 sscm with 150 sscm Ar continuously for  $\geq 2$  minutes) do measurable amounts of carbon begin to form at OCV, presumably through Ni surface-catalyzed reactions. The carbon that does form takes the form of ordered graphite, as evidenced by the single discernible feature at 1580 cm<sup>-1</sup> assigned to the graphite “G”

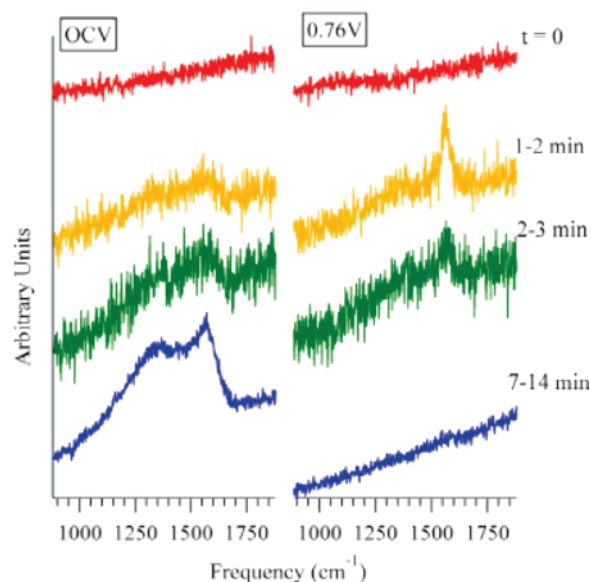


**Figure 6.** Raman spectra acquired from a Ni/YSZ porous anode operating at -1.06 V (OCV) (left) and 0.76 V (right). All experiments were carried out at 715 °C. The top, featureless traces are acquired from clean, reduced Ni/YSZ anodes operating with H<sub>2</sub>/Ar. All other spectra are acquired following a single, 5 cm<sup>3</sup> burst of butane. Following operation at a given overpotential, the anode is re-oxidized, re-reduced, and then re-characterized using H<sub>2</sub> (in Ar, see the Experimental Section) before setting a new cell potential and introducing a new 5 cm<sup>3</sup> burst of butane.

band. A representative spectrum following anode exposure to  $\sim 3$  L of CH<sub>4</sub> appears as the bottom trace of Figure 5. Carbon buildup happens monotonically as a function of time, and a timed acquisition sequence of Raman spectra monitoring carbon growth from the continuous methane feed appears in the Supporting Information (Figure S2). Analogous experiments using polarized cells failed to detect any buildup of carbon with the constant flow of methane/Ar.

This relative inactivity is likely due to methane's lack of a C–C bond and associated chemical stability in the presence of an electrocatalyst.<sup>55,56</sup> This result is consistent with previous studies of SOFC exhaust effluent that reported methane to be the most inert of all carbon-containing fuels tested.<sup>56</sup> While numerous studies have shown Ni particles to be effective at catalyzing the growth of carbon nanotubes from methane-containing atmospheres,<sup>57,58</sup> conditions promoting this process typically involve higher methane partial pressures, lower temperatures, and longer residence times than those found in operating SOFCs. Consequently, nanotube growth on SOFC anodes employed in these studies is unlikely and inconsistent with the results of in situ Raman spectra.

In contrast to methane, butane does form large amounts of deposits on Ni cermet anodes at OCV with exposures of  $\leq 5$  cm<sup>3</sup> ( $2 \times 10^{-4}$  mol). As shown in Figure 6, Raman data for a SOFC exposed to a 5 cm<sup>3</sup> burst of butane (on top of 30 sccm H<sub>2</sub> and 150 sccm Ar) show the formation of disordered graphite deposits. When the SOFC is operating, the carbon formed by butane on the Ni cermet anode persists for a time that depends upon cell potential. Higher cell potentials (and correspondingly lower currents) lead to longer carbon persistence and vice versa.<sup>42</sup> At a cell voltage of 0.76 V (right column) both the G and D peaks appear within the first minute after exposure (right column, second row). Between 1–2 min, both features have degraded, but still remain clearly discernible (right, third row). After several minutes no detectable carbon remains in the polarized anode cases (fourth row from top). At OCV, the

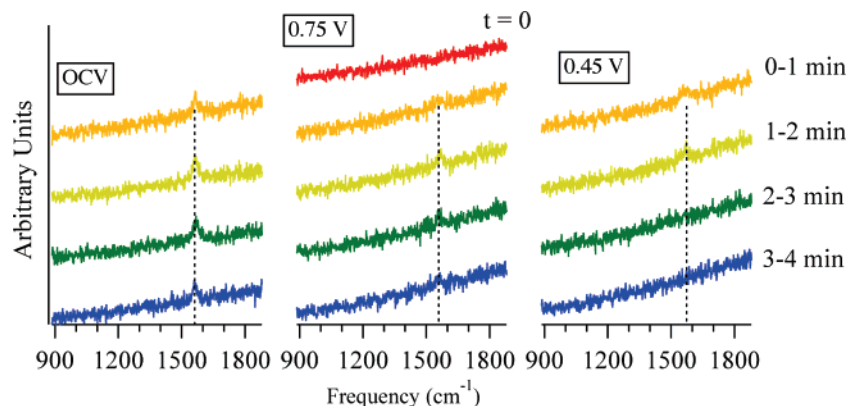


**Figure 7.** Raman spectra acquired from a Ni/YSZ porous anode operating at  $-1.05$  V (OCV) (left),  $0.75$  V (center), and  $0.45$  V (right). All experiments were carried out at  $715$  °C. The top, featureless trace of the middle column is representative and results from a clean, reduced Ni/YSZ anode. All other spectra are acquired following a single,  $5$  cm<sup>3</sup> burst of ethylene. Following operation at a given overpotential, the anode is re-oxidized, re-reduced, and then re-characterized using  $H_2$  (in Ar, see the Experimental Section) before setting a new overpotential and introducing a new  $5$  cm<sup>3</sup> burst of ethylene. S/N ratios in these short acquisitions (30 s scans) do not resolve the D peak that appears in the longer acquisition shown in Figure 8A.

graphite formed by butane remains stable indefinitely. The dramatic difference in deposit formation between methane and butane is consistent with the differences in reactivity discussed above. Although methane is a major product of butane pyrolysis, the methane vs butane comparison illustrates that the other pyrolysis products such as ethylene, propylene, and  $C_5^+$  bear the primary responsibility for deposit formation.

Figure 7 shows in situ Raman spectra acquired from a Ni/YSZ cermet anode operating with ethylene ( $C_2H_4$ ). Like that in Figure 6, the top, featureless trace results from a 30 s scan of the clean anode at OCV with a hydrogen/argon feed. A single  $5$  cm<sup>3</sup> burst of ethylene leads to the observable formation of carbon deposits on the anode as evidenced by the vibrational band that appears at  $1585$  cm<sup>-1</sup> (Figure 7, second row). Again, this vibrational band is assigned to the G mode of highly ordered graphite, and it appears during the first minute after exposure. Only in longer, higher S/N ratio spectra (acquired under OCV conditions) can a weak D signal be observed in the graphite formed on the Ni/YSZ anode with ethylene feeds (vide infra).

Under OCV conditions, the ethylene-formed carbon persists indefinitely, indicating that the graphite is stable in the absence of an oxide flux through the electrolyte. For polarized cells, the graphite formed from  $5$  cm<sup>3</sup> of ethylene disappears on the order of minutes with the rate of consumption depending upon the cell potential. At  $0.75$  V, the graphite peak intensity diminishes significantly after 2 min, although measurable intensity still exists after 4 min (Figure 7, middle panel). At  $0.45$  V, the graphite formed from the ethylene burst disappears completely after 2 min (Figure 7, right panel). This behavior indicates the importance of anode overpotentials on the rates of carbon deposit oxidation. The relatively low deposit formation tendency with ethylene is consistent with the gas-phase model predictions. Interestingly, the initial tendency of ethylene to form highly ordered graphite structures might be related to predictions that the dominant deposit precursor produced in ethylene pyrolysis is benzene.

The final fuel tested in these studies was propylene, an unsaturated hydrocarbon formed by butane pyrolysis at typical SOFC feed conditions (cf. Figure 3, bottom). In situ Raman spectra acquired from an anode exposed to a  $5$  cm<sup>3</sup> volume of propylene are shown in the Supporting Information. (Figure S3) Carbon deposits resulting from anode exposure to  $5$  cm<sup>3</sup> of propylene are markedly different from those formed by ethylene. Following the propylene burst, both the G and D (at

$\sim 1350$  cm<sup>-1</sup>) features appear for all cells operating at all potentials, although these features are especially strong under OCV

( $1.10$  V) conditions. As with carbon formed from ethylene, the propylene-formed deposits persist indefinitely under OCV conditions with no measurable change in the relative intensities of the D and G Raman bands. The relatively large D band suggests that the carbon formed from propylene is similar structurally to that formed from butane. As expected, the deposits disappear over time when cells are polarized. At a cell voltage of  $0.80$  V, the intensity of the Raman features diminish considerably after 4 min (Supporting Information, Figure S3, middle panel). At  $0.50$  V, the vibrational bands disappear completely after 2 min (Figure S3, right panel). At the lowest cell potential tested (corresponding to the highest oxide flux), the D band intensity diminishes faster than the G band intensity, suggesting that defects in the carbon deposits are most susceptible to oxidation.

Several important conclusions can be drawn from these collective results. First, methane produced from pyrolysis of higher-weight hydrocarbons is unlikely to initiate carbon deposition on Ni/YSZ cermet anodes. Second, the initial stages of carbon deposition from ethylene begin with the formation of ordered graphite as evidenced by a relatively strong band in the in situ Raman spectra at  $1585$  cm<sup>-1</sup> and the corresponding low intensity (or absent) feature at  $\sim 1365$  cm<sup>-1</sup>. This behavior might arise from two possible effects: (1) The pyrolysis rate is relatively low, leading to a slow rate of formation of gas-phase deposit precursors, allowing surface catalysis to play a larger role in the formation of ordered graphite. (2) The dominant gas-phase deposit precursor, benzene, perhaps favors graphite-like structures on the surface. Third, the fuel responsible for carbon deposits most similar to those formed by butane is propylene. This result can be anticipated in light of the predicted product distributions for the various fuels. Figure 3b shows that propylene pyrolysis, in addition to forming the unreactive species methane, will form the same unsaturated species (ethylene, acetylene, and methyl acetylene) found in butane pyrolysis (Figure 3, bottom). Since the dominant species present is unreacted propylene, the composition of those species most likely to form deposits is quite similar in butane and propylene pyrolysis.

A final comment regarding the carbon deposits deserves mentioning: despite the strongly reducing atmosphere above



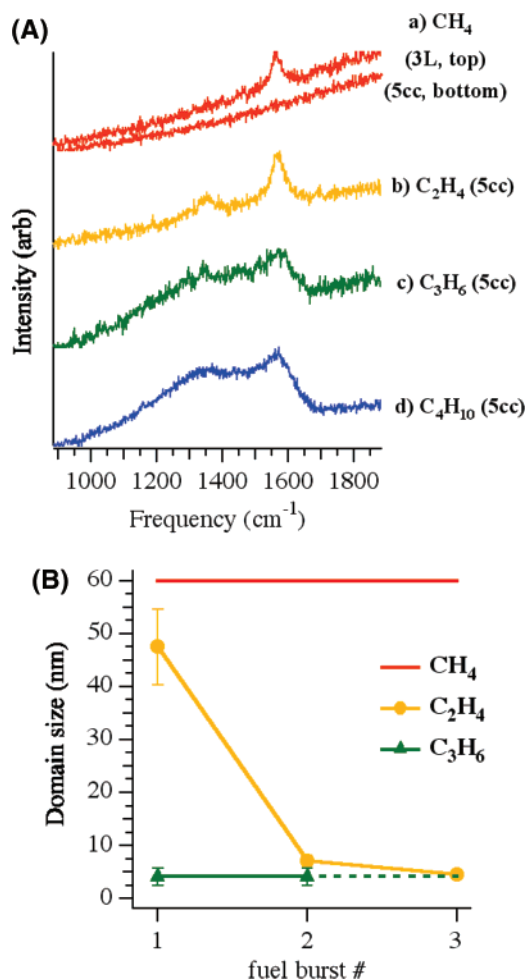


**Figure 8.** (A) High-resolution spectra of carbon deposited on anode surfaces at OCV after exposure to 5 cm<sup>3</sup> (a) methane, (b) ethylene, (c) propylene, and (d) butane. The top trace also contains the spectrum acquired from the anode following exposure to ~3 L of methane. Spectra were acquired at OCV and at a temperature of 715 °C. (B) Graphite domain size vs fuel exposure. The domain size of graphite formed with methane (a) cannot be calculated explicitly. See text for explanation. In the case of propylene fuel, graphite with a 4.1 nm domain size forms immediately. The dotted line is drawn to show the assumption that ~4 nm is the lower limit for graphite domain size. This result cannot be tested explicitly, however, as the optical window is obscured by carbon deposits after two bursts.

the SOFC anodes, Raman data never show an intensity near 3000 cm<sup>-1</sup>, indicating the absence of any -CH functional groups within the carbon deposits. The -CH stretching motion has one of the largest Raman scattering sections of any molecular vibration. The failure to observe vibrational bands associated with -CH species implies that the tetrahedrally coordinated carbon associated with the D band at 1365 cm<sup>-1</sup> is bonded to other carbon atoms and not hydrogen-terminated. This picture is consistent with the mechanisms of pyrolytic carbon growth proposed in refs 48 and 49.<sup>47,48</sup>

**Carbon Growth at OCV.** The stable carbon deposits formed on SOFC anodes at OCV provide high S/N ratio Raman spectra that allow for quantitative analysis. The spectra of anodes after exposure to each of the three hydrocarbons are shown in Figure 8A. The anode at OCV exposed to 5 cm<sup>3</sup> of methane shows no evidence of carbon deposition, but the same amount (by volume) of exposure for both ethylene and propylene produces measurable amounts of deposited carbon as evidenced by the in situ Raman spectra. (Also included in Figure 8A is the spectrum of the graphite formed by ~3 L of methane for comparison.) Spectra from both ethylene and propylene show D and G

**TABLE 1: Graphite Domain Size**

fuel	$I_D/I_G$	domain size (nm)
CH <sub>4</sub>	0	N/A
C <sub>2</sub> H <sub>4</sub>	0.074	47.5 ± 7.1
C <sub>3</sub> H <sub>6</sub>	0.855	4.1 ± 0.4
C <sub>4</sub> H <sub>10</sub>	0.898	3.9 ± 0.4

features, with the spectrum of the carbon formed from propylene evincing much more disorder than the ethylene-formed deposits. The presence of both carbon peaks allows for quantitative characterization of graphite domain size using the ratio:  $I_D/I_G = C_L/L_a$ , where  $I_x$  is the Raman peak intensity,  $C_L$  is the Raman coupling coefficient (3.504 for 488 nm light), and  $L_a$  is the domain diameter in nm.<sup>51,54</sup> Resulting domain sizes from the three hydrocarbon fuels and butane are listed in Table 1 and depicted in Figure 8B. This analysis shows clearly that as fuels increase in molecular weight, the initial graphite domains become smaller, indicating an increase in disorder. The reported domain size of carbon formed from methane represents a lower limit extrapolated from the S/N ratio of the spectra shown in Figure 5.

The ethylene data indicate that the structure of the domains changes with increased exposure. Initial exposure of the Ni/YSZ anode to ethylene results in carbon deposits with a large domain size, but unlike the carbon formed by methane (and propylene), the size of carbon domains formed by ethylene changes as a function of exposure. With the initial 5 cm<sup>3</sup> of ethylene burst, carbon growth appears slow enough that most carbon is integrated into thermodynamically stable, highly ordered structures having few defects. Subsequent additions of ethylene lead to more rapid growth of carbon deposits due to the increased nucleation sites and faster growth kinetics as predicted by autocatalytic mechanisms of carbon formation.<sup>21,59</sup> Interestingly, on a basis of per mole carbon exposure, ethylene and propylene appear to behave similarly in terms of carbon deposit structure. After 15 cm<sup>3</sup> total exposure to ethylene, the Raman spectrum of carbon deposits shows a similar  $I_D/I_G$  ratio as that from carbon deposits formed on the Ni/YSZ anode from 10 cm<sup>3</sup> of total exposure to propylene (having equivalent total carbon content). Such observations are consistent with mechanisms of carbon formation resulting from higher MW carbon deposit precursors formed during gas-phase pyrolysis.

In contrast, we note that the spectra of carbon deposits formed from methane (Figure 5) show only highly ordered graphite (with no measurable intensity near 1360 cm<sup>-1</sup>) despite the anode being exposed to up to ~10× more total carbon than is contained in 10 cm<sup>3</sup> of propylene or 15 cm<sup>3</sup> of ethylene. Taken together, these observations imply that mechanisms of carbon deposition on Ni/YSZ cermet anodes depend upon the specific identity of the fuel mixture incident upon the anode. Kinetic studies of carbon deposition have noted that deposition rates increase with hydrocarbon molecular weight.<sup>47,60</sup> Data from these studies support two different mechanisms of carbon growth on solid surfaces: (a) a growth mechanism whereby carbon grows at the edges of basal planes already present on the substrate and (b) a nucleation method in which carbon is deposited from primarily unsaturated hydrocarbon species derived from gas-phase pyrolysis reactions.<sup>48</sup> We propose that differences in these two mechanisms, surface growth vs gas-phase deposition, are directly responsible for the differences in the fuel-dependent, carbon deposit structure observed directly and in real time in the Raman data presented above.

More specifically, we believe that deposit formation from methane is governed solely by catalytic mechanisms. For other fuels, one might expect approximately comparable rates of catalytic deposit formation, but this pathway can be augmented by the formation of gas-phase deposit precursors that ultimately

**TABLE 2: Electrochemical Performance vs Exposure to Carbon-Containing Fuel**

fuel	burst <sup>a</sup>	$I_{\max}$ (mA/cm <sup>2</sup> )	$P_{\max}$ (mW/cm <sup>2</sup> )
butane	0	45	10.6
	5	23	6.9
	15	42	9.2
methane	0	22	4.5
	5	21	4.8
	15	21	4.8
ethylene	0	26	5.4
	5	24	4.9
	15	12	2.3
propylene	0	25	4.3
	5	21	4.3
	15	16	3.4

<sup>a</sup> Each burst contains 5 cm<sup>3</sup> of carbon-containing fuel on top of a H<sub>2</sub>/Ar diluent. See text for details. Complete voltammetry data appear in the Supporting Information as Figure S4. Butane and ethylene data appear in Figure 9.

form “noncatalytic” deposits. The greater the tendency of the fuel to produce higher-weight species, the larger the expected contribution from the “noncatalytic” route. Thus, one needs to account for not only for the extent of fuel conversion but also the nature of the intermediates formed (e.g., the amounts of unsaturated species formed) to properly account for the magnitude of these noncatalytic deposits.

**Effects of the Carbon Deposits on Cell Performance.** One goal of this study is to better understand the transient improvement in cell performance accompanying the creation of butane-formed graphite deposits by examining individually the effect that the primary products of butane pyrolysis have on SOFC performance. Electrochemical characterization of SOFC performance uses voltammetry to characterize SOFC performance after different amounts of exposure to the fuel of interest. During exposure, the cell is kept under OCV conditions to prevent any graphite formed from simply being oxidized away in a matter of minutes. All electrochemical measurements are conducted with hydrogen as a fuel so that overall cell performance from experiment to experiment can be compared quantitatively. The important quantities obtained from these measurements include power and current densities, and these performance benchmarks are summarized in Table 2 for all fuels studied.

Data from repeated experiments with SOFCs using butane showed that carbon formed during the very early stages of exposure led to a ~40–50% drop in power density followed by performance recovery.<sup>42</sup> (Figure 9, top panel) These results mirrored previous reports of improved SOFC performance following the formation of extensive carbonaceous deposits on Cu–ceria anodes.<sup>37,46</sup> One mechanism proposed to describe this effect requires that the carbon deposits be conducting and “wire together” isolated parts of the cermet anode.<sup>37</sup> With this model, the deposited carbon improves the current collecting ability of the anode, thus improving overall performance. Similarly, we interpret the diminished output of the SOFC observed in the experiments shown in Figure 9 to reflect the initial blockage of active sites followed by the eventual expansion of the effective anode area as the conducting carbon deposits expand.

The Raman measurements discussed in the previous section showed that methane forms small amounts of highly ordered graphitic deposits at OCV (Figure 5). In the electrochemical experiments, carbon deposition from methane is expected to be inhibited even further due to the presence of excess H<sub>2</sub>.<sup>11,47,48</sup> As expected, the electrochemical data following anode exposure to 25 and 75 cm<sup>3</sup> of methane show these small quantities of fuel to have minimal effect on the electrochemical performance of the cell. (Figure S4 in Supporting Information.) Maxima in both the current and power densities throughout the experiment vary by less than 5% from data acquired from the cell prior to

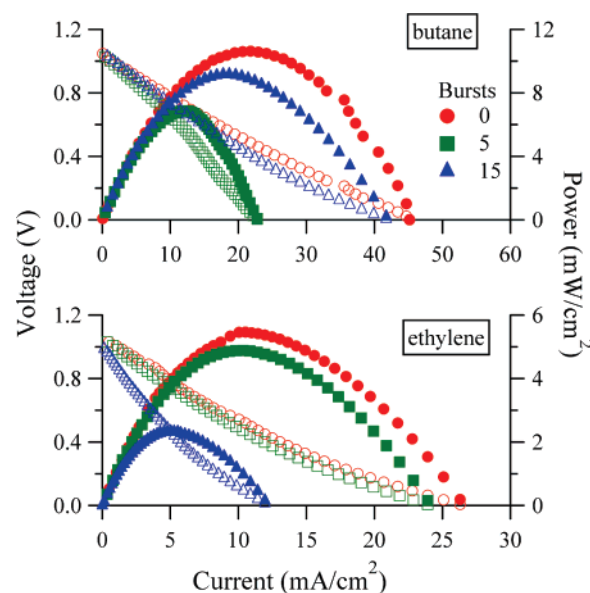


**Figure 9.** Electrochemical data acquired from cells operated with hydrogen fuel after exposure at OCV and 715 °C to 0 cm<sup>3</sup> (circles), 25 cm<sup>3</sup> (squares), and 75 cm<sup>3</sup> (triangles) of butane (top) and ethylene (bottom). The graphs show the voltammetry (open marks) and power density data (closed marks).

exposure, reinforcing the notion that methane found in the post-pyrolysis butane fuel feed is unlikely to be responsible for the observed electrochemical behavior associated with butane.

Changes in SOFC electrochemical performance as a function of ethylene exposure are evident in the bottom panel of Figure 9. After exposure to 25 cm<sup>3</sup> of ethylene, the maximum power density decreases by ~5%. This reduced performance constitutes a small change compared with the ~40% reduction in performance when the anode sees the same amount (by volume) of butane. Given the qualitative differences in the ethylene-formed graphite versus butane-formed graphite, this result is not surprising. Furthermore, SOFC anodes see 50% less total carbon for equivalent volumes of ethylene compared with those of butane. However, unlike SOFC behavior with additional added butane, continued exposure of the anode to ethylene leads to further degradation in performance. After exposure to 75 cm<sup>3</sup> of ethylene, voltammetry data show that the cell is operating at ~40% of its maximum limit with hydrogen compared with pre-ethylene exposure benchmarks. Furthermore, the SOFC performance shows no sign of recovery with additional exposure to ethylene.

The Raman spectra of carbon formed on Ni/YSZ anodes from small amounts of propylene show that this fuel creates carbon deposits that are quite similar structurally to those formed by butane. However, the electrochemical data (Supporting Information, Figure S4-d) show that structural similarities observed spectroscopically do not necessarily lead to similar impacts on electrochemical behavior. Exposure to both propylene and butane leads to the formation of carbon deposits having an average domain size of 4.9 nm (Figure 8B). The anode exposed to propylene, however, experiences degradation more closely related to those exposed to ethylene. Specifically, after 25 cm<sup>3</sup> of propylene exposure, MEA current and power densities drop by ~20%. These effects are amplified further by additional exposure; after an additional 50 cm<sup>3</sup> of propylene exposure, cell performance has decreased by 45% from the benchmark conditions defined by operation with H<sub>2</sub> prior to propylene exposure.

## Conclusions

The results presented above show that the majority products of butane pyrolysis—methane, ethylene, and propylene—form



a variety of carbon deposits that affect Ni/YSZ anode performance in various ways. Methane forms small amounts of highly ordered graphite that has little impact on cell performance relative to other fuels. Ethylene leads to more deposited carbon with slightly more disorder, and these deposits are detrimental to electrochemical performance. The structure of the carbon deposits formed by ethylene changes as a function of exposure. Propylene forms disordered carbon deposits that appear structurally similar to deposits formed by butane. The performance of cells operated with propylene continues to decline with continued exposure to the hydrocarbon fuel and does not recover. This behavior stands in contrast to the performance of cells exposed to comparable amounts of butane. Taken together, these suggest that the initial stages of carbon formation on Ni/YSZ anodes depend on the chemical nature of the incident fuel and that both the "type" of carbon formed (ordered vs disordered) and the amount of carbon deposited are important when considering the impact of graphite formation on SOFC electrochemical performance.

**Acknowledgment.** This work is supported by the Office of Naval Research MURI Grant No. 0110138816, in association with the Colorado School of Mines and CalTech. The authors specifically thank Dr. Jeffrey C. Owrutsky at the Naval Research Laboratory for insightful discussions. The authors also acknowledge helpful discussions with Prof. Bob Kee from the Colorado School of Mines who graciously provided the schematic figure of the SOFC assembly shown in Figure 1. R.A.W. acknowledges Fellowship support from the Institute for Advanced Study at Durham University (U.K.) during the early stages of manuscript preparation.

**Supporting Information Available:** Timed acquisition spectra from SOFC Ni/YSZ cermet anodes exposed to methane and propylene; complete collection of voltammetry traces whose  $I_{\max}$  and  $P_{\max}$  characteristics are summarized in Table 2. This material is available free of charge via the Internet at <http://pubs.acs.org>.

## References and Notes

- (1) Alanne, K.; Saari, A.; Ugursal, V. I.; Good, J. *J. Power Sources* **2006**, *158*, 403.
- (2) Calise, F.; Palombo, A.; Vanoli, L. *J. Power Sources* **2006**, *158*, 225.
- (3) Fontell, E.; Phan, T.; Kivisaari, T.; Keranen, K. *J. Fuel Cell Sci. Technol.* **2006**, *3*, 242.
- (4) Song, C. S. *Catal. Today* **2002**, *77*, 17.
- (5) Ormerod, R. M. *Chem. Soc. Rev.* **2003**, *32*, 17.
- (6) Holtappels, P.; De Haart, L. G. J.; Stimming, U.; Vinke, I. C.; Mogensen, M. J. *Appl. Electrochem.* **1999**, *29*, 561.
- (7) Lin, Y.; Zhan, Z.; Liu, J.; Barnett, S. A. *Solid State Ionics* **2005**, *176*, 1827.
- (8) Primdahl, S.; Mogensen, M. J. *Electrochem. Soc.* **1997**, *144*, 3409.
- (9) Deluca, N. W.; Elabd, Y. A. *J. Polym. Sci., Part B: Polym. Phys.* **2006**, *44*, 2201.
- (10) Litster, S.; McLean, G. *J. Power Sources* **2004**, *130*, 61.
- (11) Finnerty, C. M.; Coe, N. J.; Cunningham, R. H.; Ormerod, R. M. *Catal. Today* **1998**, *46*, 137.
- (12) Walters, K. M.; Dean, A. M.; Zhu, H. Y.; Kee, R. J. *J. Power Sources* **2003**, *123*, 182.
- (13) Kim, T.; Liu, G.; Boaro, M.; Lee, S. I.; Vohs, J. M.; Gorte, R. J.; Al-Madhi, O. H.; Dabbousi, B. O. *J. Power Sources* **2006**, *155*, 231.
- (14) Mallon, C.; Kendall, K. *J. Power Sources* **2005**, *145*, 154.
- (15) Yamaji, K.; Kishimoto, H.; Xiong, Y. P.; Horita, T.; Sakai, N.; Brito, M. E.; Yokokawa, H. *J. Power Sources* **2006**, *159*, 885.
- (16) Yoon, S. P.; Han, J.; Nam, S. W.; Lim, T. H.; Hong, S. A. *J. Power Sources* **2004**, *136*, 30.
- (17) Atkinson, A.; Barnett, S.; Gorte, R. J.; Irvine, J. T. S.; McEvoy, A. J.; Mogensen, M.; Singhal, S. C.; Vohs, J. *Nat. Mater.* **2004**, *3*, 17.
- (18) Pomfret, M. B.; Owrutsky, J. C.; Walker, R. A. *J. Phys. Chem. B* **2006**, *110*, 17305.
- (19) Baker, R. T.; Metcalfe, I. S. *Ind. Eng. Chem. Res.* **1995**, *34*, 1558.
- (20) He, H.; Hill, J. M. *Appl. Catal., A* **2007**, *317*, 284.
- (21) Phillips, J.; Shiina, T.; Nemer, M.; Lester, K. *Langmuir* **2006**, *22*, 9694.
- (22) Van Speybroeck, V.; Reyniers, M. F.; Marin, G. B.; Waroquier, M. *ChemPhysChem* **2002**, *3*, 863.
- (23) Wang, X. B.; Liu, Y. Q.; Zhu, D. B. *J. Nanosci. Nanotechnol.* **2002**, *2*, 33.
- (24) Laosiripojana, N.; Assabumrungrat, S. *J. Power Sources* **2007**, *163*, 943.
- (25) Chen, F. Z.; Zha, S. W.; Dong, J.; Liu, M. L. *Solid State Ionics* **2004**, *166*, 269.
- (26) Zhu, H. Y.; Colclasure, A. M.; Kee, R. J.; Lin, Y. B.; Barnett, S. A. *J. Power Sources* **2006**, *161*, 413.
- (27) Lin, Y. B.; Zhan, Z. L.; Barnett, S. A. *J. Power Sources* **2006**, *158*, 1313.
- (28) Haberman, B. A.; Young, J. B. *J. Fuel Cell Sci. Technol.* **2006**, *3*, 312.
- (29) Hecht, E. S.; Gupta, G. K.; Zhu, H. Y.; Dean, A. M.; Kee, R. J.; Maier, L.; Deutschmann, O. *Appl. Catal., A* **2005**, *295*, 40.
- (30) Matheu, D. M.; Dean, A. M.; Grenda, J. M.; Green, J. W. H. *J. Phys. Chem. A* **2003**, *107*, 8552.
- (31) Norinaga, K.; Deutschmann, O.; Huttinger, K. J. *Carbon* **2006**, *44*, 1790.
- (32) Sheng, C. Y.; Dean, A. M. *J. Phys. Chem. A* **2004**, *108*, 3772.
- (33) Gupta, G. K.; Dean, A. M.; Ahn, K.; Gorte, R. J. *J. Power Sources* **2006**, *158*, 497.
- (34) Zhu, H. Y.; Kee, R. J.; Janardhanan, V. M.; Deutschmann, O.; Goodwin, D. G. *J. Electrochem. Soc.* **2005**, *152*, A2427.
- (35) Norinaga, K.; Deutschmann, O. *Ind. Eng. Chem. Res.* **2007**, *46*, 3547.
- (36) Randolph, K. L.; Dean, A. M. *Phys. Chem. Chem. Phys.* **2007**, *9*, 4245.
- (37) McIntosh, S.; Vohs, J. M.; Gorte, R. J. *J. Electrochem. Soc.* **2003**, *150*, A470.
- (38) Bieberle, A.; Gauckler, L. J. *Z. Metallkd.* **2001**, *92*, 796.
- (39) Bieberle, A.; Meier, L. P.; Gauckler, L. J. *J. Electrochem. Soc.* **2001**, *148*, A646.
- (40) Tikekar, N. M.; Armstrong, T. J.; Virkar, A. V. *J. Electrochem. Soc.* **2006**, *153*, A654.
- (41) Dong, J.; Cheng, Z.; Zha, S. W.; Liu, M. L. *J. Power Sources* **2006**, *156*, 461.
- (42) Pomfret, M. B.; Owrutsky, J. C.; Walker, R. A. *Anal. Chem.* **2007**, *79*, 2367.
- (43) Choi, Y. M.; Abernathy, H.; Chen, H. T.; Lin, M. C.; Liu, M. L. *ChemPhysChem* **2006**, *7*, 1957.
- (44) Lu, X.; Faguy, P. W.; Liu, M. J. *Electrochem. Soc.* **2002**, *149*, 1293.
- (45) Demircan, O.; Sukeshini, M.; Pomfret, M. B.; Jackson, G. S.; Walker, R. A.; Eichhorn, B. W. Formation of Carbon Deposits from Hydrocarbon Fuels in SOFC: Towards a Mechanistic Understanding; 205th Meeting of The Electrochemical Society, 2004, San Antonio, TX.
- (46) McIntosh, S.; He, H.; Lee, S.-I.; Costa-Nunes, O.; Krishnan, V.; Vohs, J. M.; Gorte, R. J. *J. Electrochem. Soc.* **2004**, *151*, A604.
- (47) Becker, A.; Hu, Z. J.; Huttinger, K. J. *Fuel* **2000**, *79*, 1573.
- (48) Hu, Z. J.; Huttinger, K. J. *Carbon* **2002**, *40*, 617.
- (49) Costa-Nunes, O.; Gorte, R. J.; Vohs, J. M. *J. Power Sources* **2005**, *141*, 241.
- (50) Sukeshini, A. M.; Habibzadeh, B.; Becker, B. P.; Stoltz, C. A.; Eichhorn, B. W.; Jackson, G. S. *J. Electrochem. Soc.* **2006**, *153*, A705.
- (51) Ferrari, A. C.; Robertson, J. *Phys. Rev. B: Condens. Matter Mater. Phys.* **2000**, *61*, 14095.
- (52) Kakihana, M.; Osada, M. Raman Spectroscopy as a Characterization Tool for Carbon Materials. In *Carbon Alloys: Novel Concepts to Develop Carbon Science and Technology*; Yasuda, E., Inagaki, M., Kaneko, M., Endo, M., Oya, A., Tanabe, Y., Eds.; Elsevier Science, Ltd.: Oxford, U.K., 2003; pp 285.
- (53) Casiraghi, C.; Ferrari, A. C.; Robertson, J. *Phys. Rev. B: Condens. Matter Mater. Phys.* **2005**, *72*, 085401.
- (54) Matthews, M. J.; Pimenta, M. A.; Dresselhaus, G.; Dresselhaus, M. S.; Endo, M. *Phys. Rev. B: Condens. Matter Mater. Phys.* **1999**, *59*, R6585.
- (55) Mathieu, D. M.; Dean, A. M.; Grenda, J. M.; Green, J. W. H. *J. Phys. Chem. A* **2003**, *107*, 8552.
- (56) Pomfret, M. B.; Demircan, O.; Sukeshini, A. M.; Walker, R. A. *Environ. Sci. Technol.* **2006**, *40*, 5574.
- (57) Helveg, S.; Lopez-Cartes, C.; Sehested, J.; Hansen, P. L.; Clausen, B. S.; Rostrop-Nielsen, J. R.; Abild-Pedersen, F.; Nørskov, J. K. *Nature* **2004**, *427*, 426.
- (58) Li, Y. D.; Chen, J. L.; Qin, Y. N.; Chang, L. *Energy & Fuels* **2000**, *14*, 1188.
- (59) Bottcher, A.; Hennrich, F.; Rosner, H.; Malik, S.; Kappes, M. M.; Lichtenberg, S.; Schoch, G.; Deutschmann, O. *Carbon* **2007**, *45*, 1085.
- (60) Tesner, P. A. In *Chemistry and Physics of Carbon*; Thrower, P. A., Ed.; Marcel Dekker: New York, 1962; Vol. 19, pp 65.